



HAL
open science

A low-energy electron point-source projection microscope not using a sharp metal tip performs well in long-range imaging

E. Salançon, Alain Degiovanni, Laurent Lapena, Mehdi Lagaize, Roger Morin

► To cite this version:

E. Salançon, Alain Degiovanni, Laurent Lapena, Mehdi Lagaize, Roger Morin. A low-energy electron point-source projection microscope not using a sharp metal tip performs well in long-range imaging. *Ultramicroscopy*, 2019, 10.1016/j.ultramic.2019.02.022 . hal-02050666

HAL Id: hal-02050666

<https://amu.hal.science/hal-02050666>

Submitted on 27 Feb 2019

HAL is a multi-disciplinary open access archive for the deposit and dissemination of scientific research documents, whether they are published or not. The documents may come from teaching and research institutions in France or abroad, or from public or private research centers.

L'archive ouverte pluridisciplinaire **HAL**, est destinée au dépôt et à la diffusion de documents scientifiques de niveau recherche, publiés ou non, émanant des établissements d'enseignement et de recherche français ou étrangers, des laboratoires publics ou privés.

A low-energy electron point-source projection microscope not using a sharp metal tip performs well in long-range imaging

Evelyne Salançon, Alain Degiovanni, Laurent Lapena, Mehdi Lagaize and Roger Morin

CINaM, Aix-Marseille Univ, CNRS, UMR 7325

Abstract

A low-energy electron point-source projection microscope that uses a metal/insulator structure as source instead of a sharp metal needle is presented. By combining this source with an electron optical lens and a high spatial resolution image detector, performances comparable to those of a normal electron projection microscope are easily accessible and presented here. The accessible electron energy range extends from 100eV to 1000eV. In the example presented here, instead of the usual near-field source-object distance, long-range imaging at a distance of about 600 μ m is achieved.

1- Introduction

The normal low-energy electron point-source projection microscope [1,2,3,4] is a lensless system where an electron point source illuminates a perforated object, and the “physical shadow” of the object is recorded on a more distant fluorescent screen. The so-called physical

shadow corresponds to the interference between the reference wave that comes directly from the source and the object wave that results from object scattering. This Fresnel interference pattern is an electronic hologram of the object. Numerical reconstruction yields an image of the object in its position during the recording [5,6,7]. The projection microscope is known to reach a magnification of about 10^5 with an experimental spatial resolution of about 1nm [8,9,10]. These characteristics are obtained using electron sources that consist of ultra-sharp metal tips with a tip radius of about 10nm [11,12]. The magnification of the microscope, G , directly depends on the distances between point source and object d , and between point source and screen $D + d$:

$$G = \frac{D+d}{d} \quad (1.1)$$

For ultra-sharp tips, the source-to-object distance d can be decreased down to sub-micrometer level while retaining point-source behavior and large enough magnifications, without running the risk of the tip crashing into the object. We recently introduced an electron source [13,14,15] based on emissions from a single insulator crystal of celadonite deposited at the apex of a 10 μ m-diameter carbon fiber. In terms of the wave, this provides a point-source although, physically-speaking, the source is wide. The term wide-point-source can be used, since the source optically corresponds to a point-source but its geometry is wide. The wide-point-source cannot get closer than about 50 μ m from an object without any risk of crashing into it. Despite the weak projection magnification resulting from this limitation and some negative features described below, this source also presents major advantages compared to sharp metal tips. For example, it can operate in a relatively poor ultra-high vacuum or emit with wide emission angles, a crucial parameter for high-resolution imaging. To compensate for the weak

magnification, a setup consisting of two Einzel lenses is added to the imaging system to provide images of any plane between the source and the entrance of the first lens. At electron energy of 100eV, a lens setup magnification of x70 was measured [16]. Combining projection and electronic lenses should therefore lead to magnification greater than $\times 10,000$. This enables projection microscopy to work at high source-object distances while keeping the field on the object stable and limiting image distortions [17,18,19,20,21].

A microchannel-plate/fluorescent-screen assembly with a spatial resolution of about 100 μm is the typical detection system used in low-energy electron projection microscopy. Recently, we showed that the resolution of the detection is 15 μm [22,23] when a counting technique is used with a dual-stage microchannel plate (MCP), allowing this detection technique to deliver a resolution of some nanometers.

In this paper, we provide details of the source's construction, the microscope setup and the method used to record holograms. Various aspects of resolution on the images after reconstruction are also discussed, assuming normal working conditions with a source-to-object distance of 600 μm .

2- Experimental setup

The design of the electron point-source projection microscope is described in figure 1 and an industrial drawing is provided in figure 2. The microscope operates under vacuum maintained with an ionic pump.

The electron source is a 10 μm -diameter carbon fiber with a celadonite crystal at its apex [15].

This source and its characteristics are described in section 2.1.

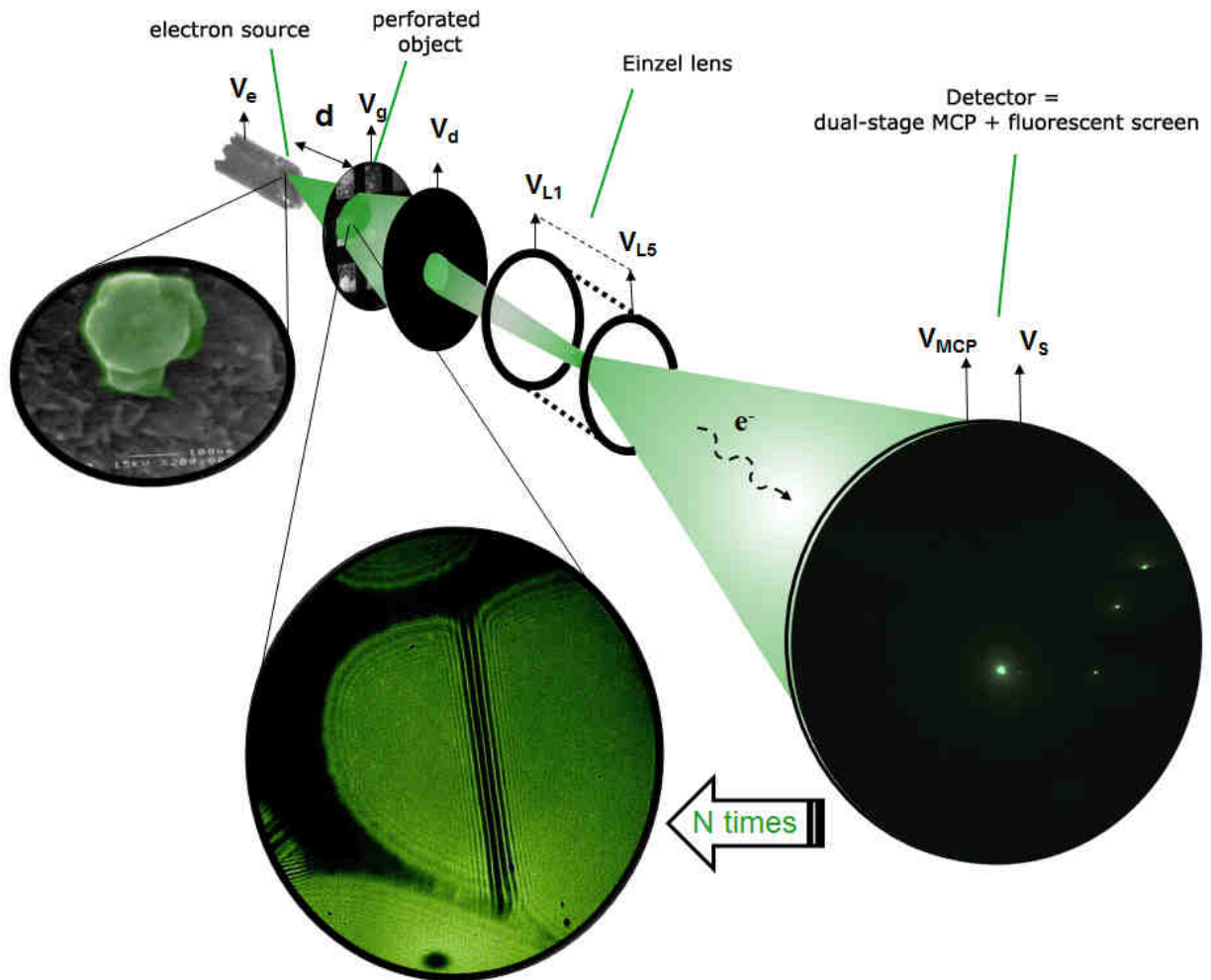


Figure 1: Experimental design. The electron source provides an electron energy range from 100 to 1000eV. The source-to-object distance, $d \geq 50\mu\text{m}$; the source-to-lens entrance distance is about 3cm. The two-Einzel-lens system provides a magnification of x70. The resolution of the dual-stage MCP assembly is about 15 μm in counting mode.

The source-to-object distance d , is controlled by a piezoelectric actuator (MS30 from Mechnics) providing distance control from 100nm to 2.5cm. Because of the source diameter, the minimum reachable source-to-object distance is about $d \gtrsim 50\mu m$. The perforated object commonly used is a holey or lacey carbon film sufficiently perforated to obtain scattered-object and reference waves to the rear of the object. The object is generally connected to the electrical ground through a picoammeter.

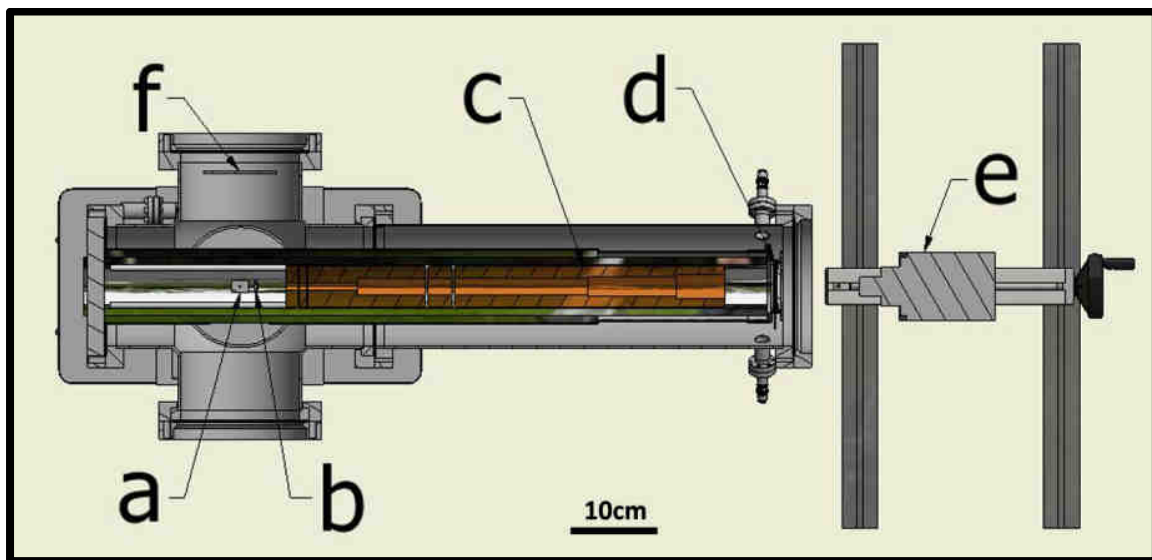


Figure 2: Industrial drawing of the point-source projection microscope; (a) source support, (b) perforated object, (c) electrostatic lens, (d) detector: dual-MCP/fluorescent-screen assembly, source-to-detector distance: = $66cm$, (e) camera and its lens, (f) direct fluorescent screen, source-to-screen distance $D_0 = 12cm$.

The source is mounted on an axis fixed on a rotating flange to orient the beam either towards a fluorescent screen alone or towards the lens. The object is fixed on the same axis and rotates with the source.

The entrance to the lens is approximately 30mm from the source depending on the source size and on the translation position. At this stage, the pure projection magnification is about x300.

The lens consists of two Einzel lenses. It is described in section 2.2, together with the methods used to enlarge the projection image and to improve lens performance in our configuration .

Finally, the detector is composed of a dual-stage MCP / fluorescent screen assembly from Hamamatsu (F2225-21P). It has a diameter of 4cm and it is placed 6cm from the lens exit fixed around a mu-metal cylinder. A window flange is 4cm from the screen. A camera Hamamatsu Orca flash 4.0 films the fluorescent screen through a Canon optical lens, with a 16-bit dynamic range. In analog imaging mode, which allows continuous image acquisition, the spatial resolution of the detector is about 150 μm . In counting imaging mode, each electron impact is translated as '1' and their accumulation yields a detector resolution of about 15 μm [23]. This system and its operation are described in section 2.3.

2.1- Electron point-source: preparation and characteristics

The electron source is composed of one celadonite crystal at the apex of a 10 μm diameter carbon fiber. For ease of manipulation, 2 or 3mm of the fiber are left projecting from a 90 μm inner diameter stainless steel tube where it has been inserted, as carbon fiber breaks very easily. The fiber is glued to the tube with silver lacquer. The larger tube is inserted into a Macor[®] support fixed on a rotating flange (see figure 3). The celadonite crystal is deposited at the apex of the carbon fiber (figure 4a) when all elements have been glued together and are in contact.

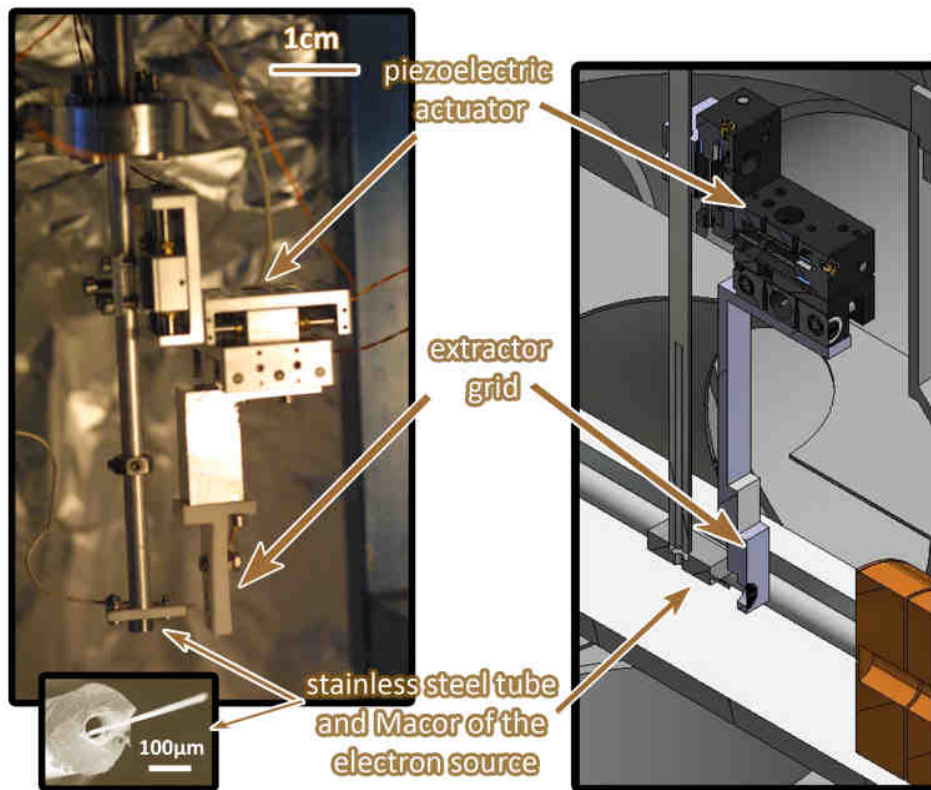


Figure 3: Photograph and industrial drawing of the electron source in front of the object, a holey carbon film on a copper grid

The mineral celadonite is an insulator crystallized in the monoclinic system (figure 4b). When celadonite is ground, the overall crystal shape is a rectangular slab (1000 nm x 500 nm x 50 nm). The celadonite crystal is deposited using a glass capillary with a tip aperture diameter of 10µm minimum (figure 4c). The crystal's powder is first dispersed under ultra-sound in deionized water. The capillary is filled with dispersed celadonite water and slight pressure is applied to the wide end of the capillary to form a small drop to buffer the apex of the carbon fiber. To obtain at least one crystal in the deposited water drop, dissolution requires about 0.2mg of celadonite

powder in 10mL deionized water. Tens of electron sources were prepared in this way, all of them emitting.

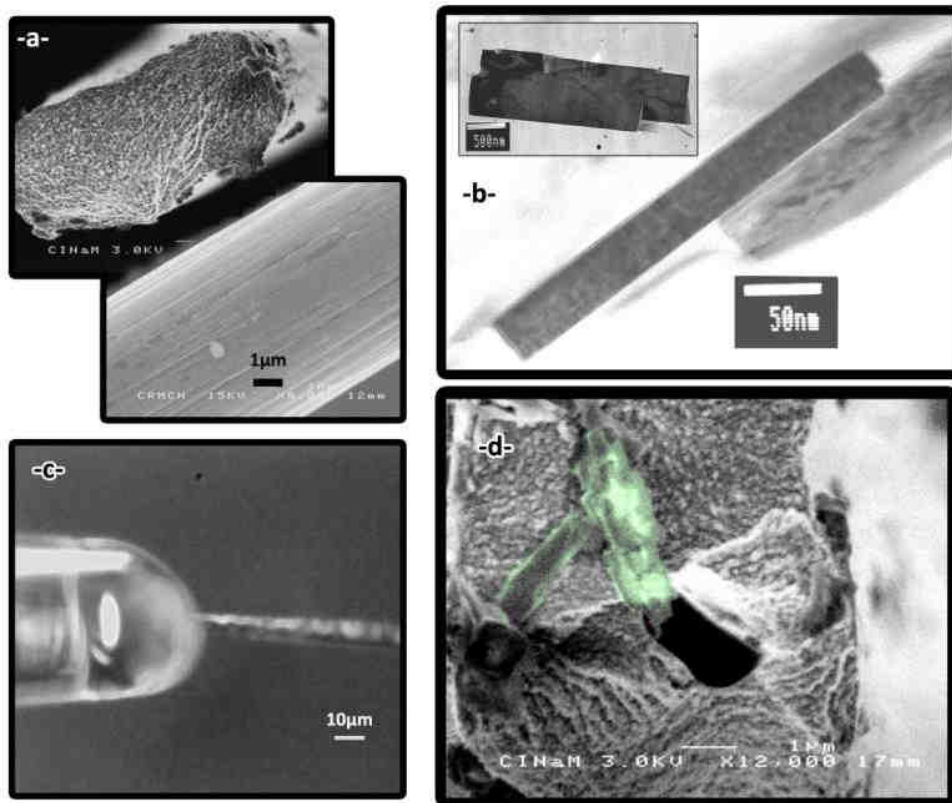


Figure 4: a- Scanning electron microscopy images of the 10µm diameter carbon fiber; b- Transmission electron microscopy image of a celadonite crystal; c- Under an optical microscope, buffering of the apex of the carbon fiber using a glass capillary filled with deionized water containing dispersed celadonite powder (0.2mg in 10mL); d- Scanning electron microscopy image of one celadonite crystal at the apex of the carbon fiber.

This electron point-source follows a Fowler-Nordheim regime over a 10 orders-of-magnitude current range with a saturation regime at the highest currents (typically 100nA and 500V applied voltage). Thus, the process observed is electric field emission. Yet the applied electric

field is only some $V/\mu\text{m}$. Since field emission requires an electric field of some V/nm this means that there is an electric field enhancement at the metal/insulator interface [15].

Typically, when the object (the perforated carbon layer) is 1mm from the source, several hundred volts are applied to trigger the emission. Figure 5 shows three typical $I(V)$ curves. The green curve corresponds to the electrical characterization of the source used in this article. Electrical measurements were made with a source-to-object distance of about $d = 600\mu\text{m}$. Intensity is measured between the object and the electrical ground.

The experiments presented here were performed with the same source-to-object distance of $600\mu\text{m}$. According to the imaging mode chosen, electron intensity is tuned through the voltage applied to the source. However, emission intensity could also be tuned through the source-to-object distance chosen. Moving the object closer to the source increases the electric field; emission intensity increases even if the voltage is constant. This tuning mode is not used here, due to a possible emission site change discussed in Results and discussion.

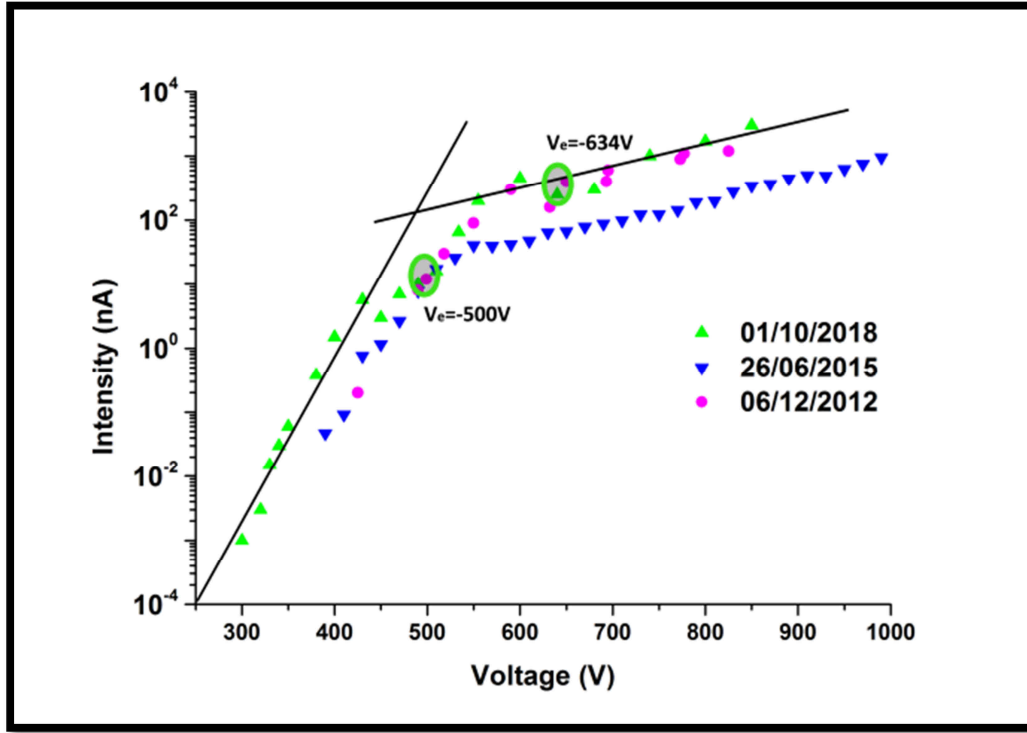


Figure 5: Typical $I(V)$ curves obtained for three different structures. The green curve represents the electrical characterization of the source used in this article. The source-to-object distance is about $d = 600\mu m$.

The brightness of a particle source is given by:

$$B(E, \Delta E) = \frac{I(E \pm \Delta E)}{S \times \Omega} \quad (2.1),$$

with $I(E \pm \Delta E)$ the emission intensity of the source at E energy with a given relative energy dispersion $\Delta E/E$. S is the surface of the emission site and Ω the solid angle of the emission.

Here, the brightness is about $B = 10^{10} A \cdot cm^{-2} \cdot sr^{-1}$, comparable to field emission tips but with a larger emission angle $2\alpha \approx 60^\circ$ ($\Omega \sim 1sr$), double that of the tips. This high solid angle improves spatial resolution [7] of the microscope, theoretically given by the Abbe diffraction

limits $\varepsilon = \frac{\lambda}{2.N.A.}$ where λ is the wavelength and $N.A. = \sin \alpha$, the numerical aperture of a projector with α the half emission angle.

The source can even operate under a relatively poor vacuum: it still works at $P = 10^{-2} \text{ mbar}$.

However, its life-time and its stability increase with good vacuum conditions, so pressure is maintained at $P = 10^{-8} \text{ mbar}$ for microscopy. The robustness of the source and its ability to work in poor vacuum conditions are great advantages in terms of experimental time and the risk of damage to the source.

Results shown here are from experiments performed at $P = 10^{-8} \text{ mbar}$ maintaining the same source-to-object distance $d = 600 \mu\text{m}$; the emitted intensity is tuned by changing the voltage applied to the emitter.

2.2- Einzel lens magnification

The two Einzel lenses are illustrated in figure 6: the length of the system is 54.5cm; the entrance aperture is a diaphragm of 1mm and the exit has a diameter of 3cm.

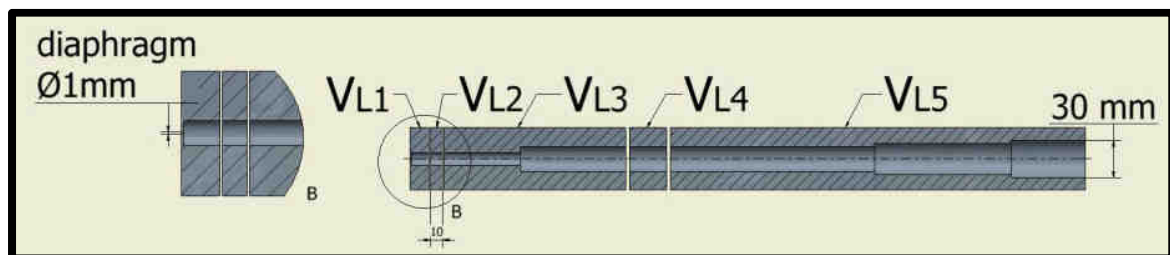


Figure 6: The two- Einzel-lens scheme. The scale bar indicates 10mm. The entire length is about 54.5cm, the aperture diameter is 1mm and the exit diameter is 3cm.

Because of the large number of voltages involved in the electron optical system, we fixed 3 voltages at zero (V_{L1}, V_{L3}, V_{L5}) and varied 2 voltages (V_{L2}, V_{L4}). In this experimental approach, two successive inversions of images were observed. Figure 7 schematically shows how the projection image is magnified, with P_0 the pure projection plane and P_2 the detector plane. The focal lengths, and therefore plane P_0 , are unknown. However we know that P_0 stands between the source and the entrance to the lens and that Einzel lenses are convergent with a focal length that decreases with the central voltage. First, projection is magnified by the first lens and the image is reversed; then the second lens reverses the image once again. Microscope magnification is given by the ratio: $G_T = G_0 \times G_L$ between a pure projection magnification $G_0 = \frac{S_{P_0}}{S_0}$ and the lens magnification $G_L = \frac{S_{P_2}}{S_{P_0}}$, where S_0, S_{P_0}, S_{P_2} are the sizes of the object and its images in planes P_0 and P_2 .

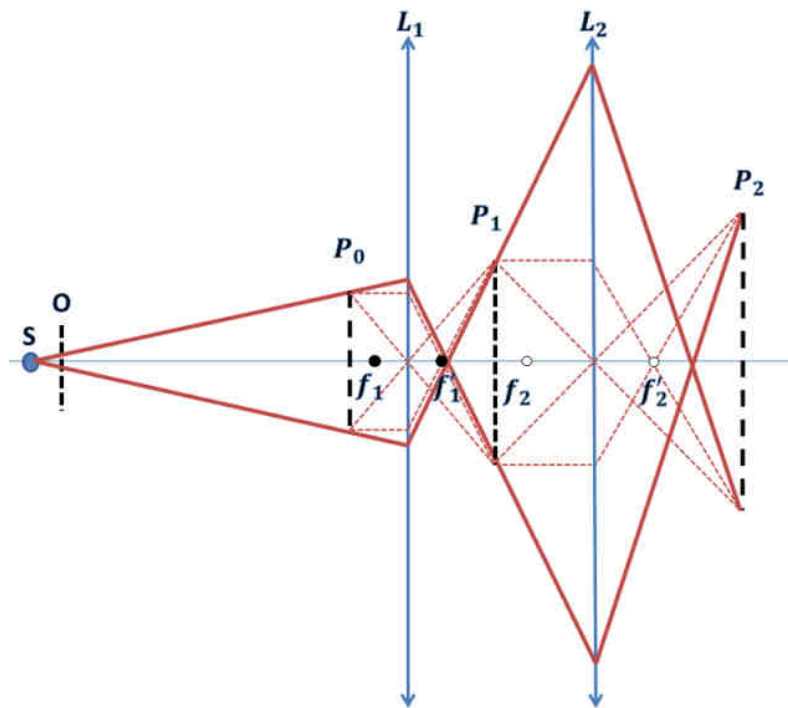


Figure 7: Electrostatic optical rays from the source to the screen with s : the source, O : the perforated object, P_0 : the object projection plane, P_1 : image of P_0 by lens L_1 , P_2 : image of P_1 by lens L_2 produced on the screen.

A typical magnification obtained with the lenses of our experimental setup is shown in figure 8. The lens potentials of this specific image are indicated in the caption as an example. For figure 8c, with an emission voltage of $V_e = -634V$: $V_{L2}=-632V$ and $V_{L4}=-590V$ to reach a magnification of $G_T = 25400$. This is almost 20 times the direct projection image obtained for figure 8b, a classic result for this setup.

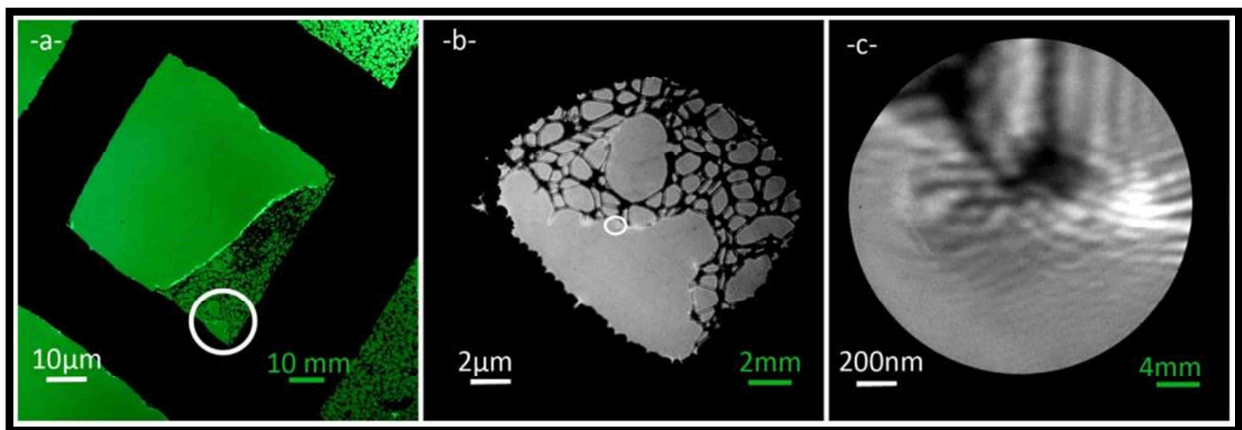


Figure 8: Physical projection images of the same object in analog mode. White scale bars represent the sizes of the object, and green scale bars the screen sizes. (a) Fluorescent screen, projection distance $D_0 = 12\text{ cm}$, $V_e = -780V$, $G_0 = 199$. The white circle indicates the part shown in figure (b). (b) Dual-MCP/fluorescent-screen assembly without lens action, projection distance $D = 66\text{ cm}$, $G_p = 1104$, $V_e = -634V$, $V_{MCP} = 1.2\text{ kV}$, $V_{screen} = 5.2\text{ kV}$, $t_{exp} = 10\text{ ms}$ (mean of 50 frames). The white circle indicates the part shown in figure (c). (c) Dual-

MCP/fluorescent-screen assembly with lens action, $G_T = 25400$, $V_e = -634V$, $V_{MCP} = 1.2kV$, $V_{screen} = 5.2kV$, $t_{exp} = 100ms$ (mean of 50 frames), $V_{L2} = -632V$, $V_{L4} = -590V$.

Here, the source-to-object distance is about $d = 600\mu m$: this is deduced from the magnification given on the short projection in figure 8a. The carbon grid lattice corresponds to $(1.7 \pm 0.1)cm$ on the screen placed at a distance $D_0 = 12cm$ from the source, the grid lattice measures $84.7\mu m$, so the magnification $G_0 = (200 \pm 10)$ and $d \simeq \frac{D_0}{G_0} = (600 \pm 30)\mu m$.

At this source-to-object distance, the part of the projection of the object seen on the lens screen is shown in figure 8b, where the magnification is $G_p = \frac{66.10^{-2}}{600.10^{-6}} \approx 1100$. The magnification measured on the image is 1104, so the source-to-object distance is found with a good confidence level.

2.3- Dual-stage microchannel-plate/fluorescent screen assembly detector

The detector-resolution of the classic point-source projection electron microscope is about $100\mu m$. This is equivalent to the Point-Spread-Function of a microchannel plate [24] or to the single-event answer of one pitch of the microchannel plate. One way to improve spatial detector-resolution is to record images in counting mode [23]. In this mode, the position of each electron's impact on the detector is determined. The complete detection system is presented in figure 9. The amplification ratio of the dual-stage microchannel plate depends on $V_{MCP} = (V_{out} - V_{in})$. Here, the detector entrance is connected to the electrical ground $V_{in} = 0V$. The starting amplification given by the manufacturer of the MCP is from about 10^3 at $1 keV$ to some 10^6 at $2 keV$. The analog imaging mode operates at an amplification of about 10^3 ($V_{MCP} \leq$

1.2kV) and the counting imaging mode at a higher amplification ($1.5 \leq V_{MCP} \leq 2kV$). To detect every single event, a dual-stage microchannel plate must be used but the electron flux must also be sufficiently low: if events follow each other too closely, they cannot be counted. There are almost 1.8 million channels on the first microchannel plate, which has a diameter of 4cm. Impacted by one electron, each can produce a micrometric stain. The electron is counted at the stain's center of mass. Increasing video frequency would substantially reduce imaging time. Here, the minimum exposure time for the camera is $(t_{exp})_{min} = 3.02ms$. For the counting imaging mode, the maximum dose acceptable is about 10,000 hits per frame: $I_{screen} = 1.6 \times 10^{-19} \frac{10^4}{3.02 \times 10^{-3}} = 0.5pA$.

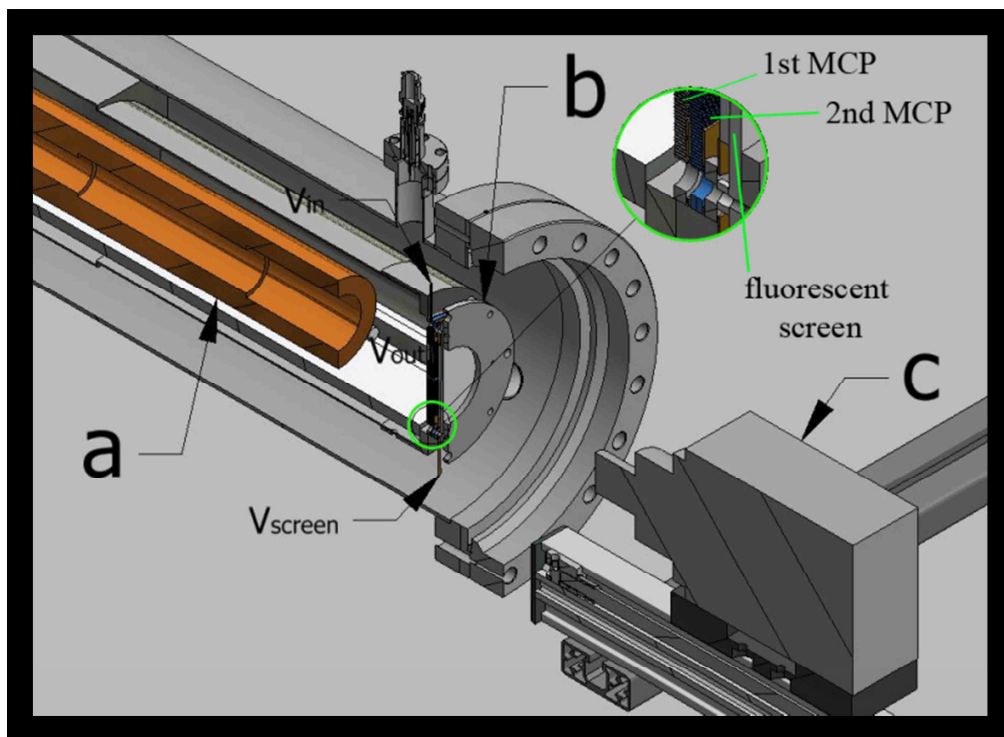


Figure 9: Technical drawing of the complete detection system. (a) Electrostatic lens; (b) dual stage microchannel-plate/fluorescent-screen assembly with the entrance of the first MCP

connected to the electrical ground ($V_{in} = 0V$), the exit of the second MCP connected to V_{out} and the isolated fluorescent screen connected to V_{screen} (c) camera and its optical lens.

3- Results and discussion

The detector-resolution is known to be about $\eta=15\mu\text{m}$ in counting imaging mode and $\eta=150\mu\text{m}$ in analog imaging mode [23,24,25]. Under microscope magnification, G , this detector-resolution should lead to a microscope-resolution of η/G . In our example, the magnification is about $\times 25.400$, which should give a microscope-resolution of 6nm in analog mode and 0.6nm in counting mode. To see whether this is the case, the microscope-resolution is estimated by plotting the profile of gray-level intensity along a line placed at the edge of the object in the reconstruction of the hologram (figure 10). The microscope-resolution is equivalent to the width of this edge.

To compare the microscope-resolutions obtained in analog and in counting mode, the same image is recorded in both modes. However, the (2048×2048) pixel CMOS device of the camera does not allow every channel of the entire microchannel plate to be resolved. The answer is to zoom onto one part of the screen. The counting image is then incorporated into the analog image, as shown in figure 10. An analog image is first recorded (figure 10a) in 25sec (mean of 50 frames of $t_{exp} = 500\text{ms}$). Then, the image of the object is positioned at the center of the screen. The focal length of the camera lens and the camera position are changed to zoom on the object. A $(7 \times 7) \text{mm}^2$ area of the screen is then filmed at a high imaging rate: here, 42,000 images of $t = 3.02\text{ms}$ every 30ms form the counting image obtained in figure 10b. At $V_e = -500V$, the emission intensity is about 10nA (figure 5), yielding 10pA after the

diaphragm. Just a small part represented by the white circle in figure 8b illuminates the whole screen: the intensity arriving on the screen is about 0.1pA: 80 hits per frame ($(7 \times 7) \text{ mm}^2$ of the screen). This counting imaging mode is time-consuming: it took 34min to record figure 10b. The image in figure 10c is realized by incorporating the figure 10b ($7 \times 7) \text{ mm}^2$ counting image into the figure 10a ($4 \times 4) \text{ cm}^2$ analog image.

The detector-resolution on the counting image is not $15\mu\text{m}$ here because it is blurred by a mechanical drift of the object towards the source position. The measurements performed on 10b give a recording detector-resolution of about $48\mu\text{m}$, which corresponds to a mean drift of $16\text{nm}/\text{sec}$ between the source and the object.

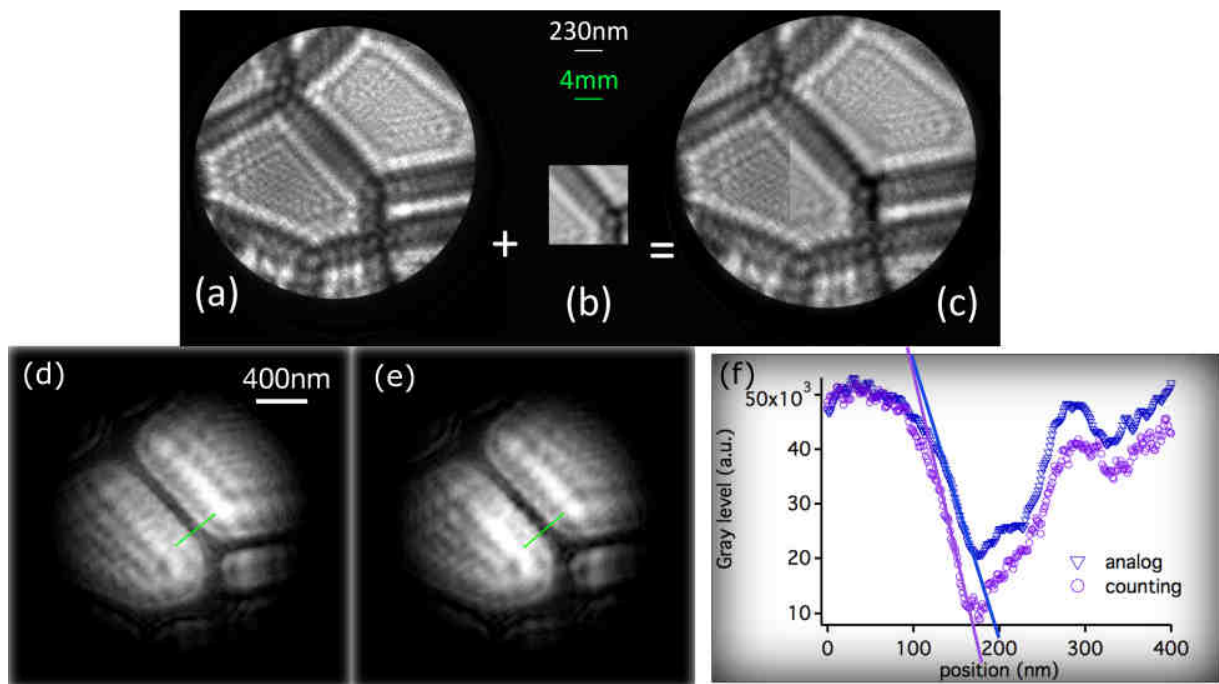


Figure 10: (a) Analog image of a carbon membrane physical shadow. Projection distance $D = 66\text{cm}$, with lens action, $V_e = -500\text{V}$, $V_{out} = 1.5\text{kV}$, $V_s = 5.5\text{kV}$, $t_{exp} = 500\text{ms}$ (mean of 50 frames), $V_{L2} = -500\text{V}$, $V_{L4} = -435\text{V}$, $G_T = 17400$; (b) Counting image of a part ($1\text{cm} \times 1\text{cm}$)

of the screen. Projection distance $D = 66\text{cm}$, with lens action, $V_e = -500\text{V}$, $V_{out} = 1.8\text{kV}$, $V_s = 5.8\text{kV}$, $t_{exp} = 3.02\text{ms} \times 42000$, $V_{L2} = -500\text{V}$, $V_{L4} = -435\text{V}$, $G_T = 17400$; (c) Image (b) is incorporated in image (a); (d) Reconstruction of (a); (e) Reconstruction of (c), with counting image incorporated into analog image; (f) Gray-level intensity profiles taken along the green lines in (d) and (f).

Holograms are reconstructed by re-propagating a modeled reference wave modulated with the hologram to find the object wave in the plane of the object [6,19]. Figure 10d results from the analog imaging and figure 10e from a mix of the analog and the counting imaging shown in figure 10c.

The contrast, $\Gamma = \frac{I_{max} - I_{min}}{I_{max} + I_{min}}$, of the reconstruction is better where the counting image is incorporated. Profiles obtained on figure 10f give $\Gamma = 0.33$ for the analog image and 0.66 for the counting image. The microscope-resolution found on this image is about 40nm in analog mode and 30nm in counting mode (see figure 10f). We can conclude that due to mechanical drift, the analog image achieved in 25s leads to a microscope-resolution of about 40nm and the counting image achieved in 34min leads to a microscope-resolution of about 30nm.

Alignment and the first analog images take only a few minutes, but there are still some practical challenges. First, to capture the best counting image, the object has to be stable. Second, monitoring an object during approach can be difficult because the emission can sometimes show two sources under the same crystal. During the source-to-object approach, either both sources emit or one dominates the other. Figure 11 shows two sources working at the same time. Different image centers are observed from the two sources: images are drifted and

superimposed. The distance between sources is about $5\mu\text{m}$, corresponding to the drift between images. This inter-source distance is particularly high compared to distances previously measured [14]. Here, two closed crystals seem to emit at the same time. However, when the electric field is stable, the source doesn't change. Several point-sources can emit from one crystal, but under a given electric field condition, one of them emits preferentially. Therefore the co-existence of two sources means that the counting image obtained can be different from the image chosen before the source-to-object approach when the electric field shape changes. It is hard to anticipate how the image will change before beginning the lengthy counting procedure.

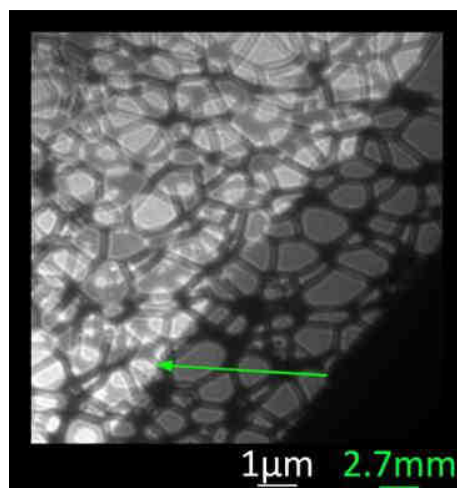


Figure 11: Projection image from two sources.

To overcome this problem, an image is first recorded in analog mode with low lens magnification and without changing the source-to-object distance before moving to counting imaging mode.

4- Conclusion

This paper describes a new design for a low-energy electron point-projection microscope with an insulator crystal as source instead of a sharp metal needle, an electron optical system, and a high-spatial-resolution detector.

The source used is an insulator/metal interface emitter formed by a celadonite crystal deposited on the apex of a 10 μ m diameter carbon fiber. The robustness and the great brightness of this source, combined with an accessible high-intensity range, make it a good candidate for electron microscopy. However its shape is a limitation to its use for classic projection microscopy, because it is difficult to manipulate at less than some tens of micrometers from an object. The projection is thus combined with electrostatic lenses to reach magnification of about 10⁵. High electron spatial detector-resolution is achieved using a dual-stage microchannel-plate/fluorescent-screen assembly. This technique affords spatial detector-resolution close to 15 μ m, the lattice parameter of the microchannel plate, but requires a long imaging time. An example combining analog imaging on a large field with counting imaging on a smaller field is shown. In the example given in this article, the source-to-object distance is 600 μ m, magnification reaches x25,000 and the resolution of the microscope is about 30nm. Both emission site changes and object drifts are observed during the lengthy imaging.

In conclusion, the celadonite source emitter combined with Einzel lens performs comparably to a point projection microscope. Moreover, its source can work under poor vacuum conditions, its robustness reduces risk during manipulation and contributes to its long life-time, and its high cone angle promises better resolution for the microscope. All of these advantages open new horizons for projection electron microscopy. With its potential for long-range imaging, the

celadonite-source projection microscope holds promise for charge reduction and ease of manipulation during imaging.

Acknowledgment

The authors would like to thank Marjorie Sweetko for improving the English of this article.

-
- [1]- W. Stocker, HW Fink and R. Morin, *Ultramicroscopy* **31**, 379 (1989)
 - [2]- R. Morin, *Microscopy Microanalysis Microstructures* **5**(4-6), 501 (1994)
 - [3]- H. W. Fink, W. Stocker, H. Schmid, *Phys. Rev. Lett.* **65**, 1204 (1990)
 - [4]- H.J. Kreuzer, K. Nakamura, A. Wierzbicki, H.W. Fink, H. Schmid, *Ultramicroscopy* **45**, 381 (1992)
 - [5]- X.M.H. Huang, J.M. Zuo, J.C.H. Spence, *Appl. Surf. Science* **148**, 229-234 (1999)
 - [6]- J. Bardon, A. Degiovanni, V. Georges, and R. Morin, *Ultramicroscopy* **92**, 133 (2002)
 - [7]- T. Latychevskaia, *Ultramicroscopy* **175**, 121 (2017)
 - [8]- E. Steinwand , J.-N.Longchamp, H.-W.Fink, *Ultramicroscopy* **110**, 1148 (2010)
 - [9]- A. Eisele, B. Völkel, M. Grunze, A. Gölzhäuser, *Zeitschrift für Physikalische Chemie* **222**(5-6), 779 (2008)
 - [10]- J.N. Longchamp, S. Rauschenbach, S. Abb, C. Escher, T. Latychevskaia, K. Kern, HW Fink, *Proceedings of the nat. academy. of Sciences of USA* **114**(7), 1474 (2017)
 - [11]- Chang CC, Kuo HS, Hwang IS, Tsong TT, *Nanotechnology* **20**(11), 115401 (2009)
 - [12]- K. Nomura, T. Nagao, BL. Cho, H. Katsuda, T. Matsumura, C. Oshima, *JVST B* **27**(6), 2432 (2009)
 - [13]- J. Rech, O. Grauby, and R. Morin *JVST B* **20**, 5-9 (2002)
 - [14]- R. Daineche, A. Degiovanni, O. Grauby, and R. Morin, *Appl. Phys let.* **88**, 023101 (2006)
 - [15]- E. Salançon, R. Daineche, O. Grauby, and R. Morin, *JVST B* **33**, 030601 (2015)
 - [16]- C. Constancias and R. Baptist, *J. Vac. Sci. Technol. B* **16**, 841 (1998).
 - [17]- Beyer A , Goelzhaeuser A , *Journal of Physics- Condensed Matter* **22**, 343001, (2010)
 - [18]- Hwang IS, Chang CC, Lu CH, Liu SC, Chang YC, Lee TK, Jeng HT, Kuo HS, Lin CY, Chang CS, Tsong TT, *New Journ. Phys.* **15** (2013)
 - [19]- V. Georges, J. Bardon, A. Degiovanni, and R. Morin, *Ultramicroscopy* **90**, 33 (2001)
 - [20]- M. Prigent, P. Morin, *J. of Phys. D- Applied Physics* **34**(8), 1167 (2001)
 - [21]- M. Prigent, P. Morin, *J. of Microscopy – Oxford* **199**, 197 (2000)
 - [22]- A.S. Tremsin, J.V. Vallerga, J.B. McPhate, O.H.W. Siegmund, W.B. Feller, L. Crow, and R.G. Cooper, *Nuclear Instruments and Methods in Physics Research A* **592**, 374 (2008)
 - [23]- Salançon E, Degiovanni A, Lapena L and Morin R, *Rev. Sci. Instrum.* **89**, 043301 (2018)
 - [24]- G. Kim, K. Isaacson, R. Palmer, R. Menon, *Applied Optics* **56**, 6450-6456 (2017)